

# Observation of terahertz spin-Hall magnetoresistance in insulating magnet YIG/Pt

P. Kubaščík<sup>1</sup>, Richard Schlitz<sup>2</sup>, Oliver Gueckstock<sup>3,4</sup>, Oliver Franke<sup>3</sup>, Martin Borchert<sup>5</sup>, Gerhard Jakob<sup>6</sup>, K. Olejník<sup>7</sup>, A. Farkaš<sup>1,7</sup>, Z. Kašpar<sup>1,7</sup>, J. Jechumtál<sup>1</sup>, M. Bušina<sup>1</sup>, E. Schmoranzarová<sup>1</sup>, P. Němec<sup>1</sup>, Martin Wolf<sup>4</sup>, Y. Z. Wu<sup>8,9</sup>, Georg Woltersdorf<sup>10</sup>, Mathias Kläui<sup>6</sup>, Piet W. Brouwer<sup>3</sup>, Sebastian T.B. Goennenwein<sup>2</sup>, Tobias Kampfrath<sup>3,4</sup>, Lukáš Nádvořník<sup>1,\*</sup>

1. Faculty of Mathematics and Physics, Charles University, 121 16 Prague, Czech Republic
  2. Department of Physics, University of Konstanz, Konstanz, Germany
  3. Department of Physics, Freie Universität Berlin, 14195 Berlin, Germany
  4. Department of Physical Chemistry, Fritz Haber Institute of the Max Planck Society, 14195 Berlin, Germany
  5. Max Born Institute for Nonlinear Optics and Short Pulse Spectroscopy, 12489 Berlin, Germany
  6. Institut für Physik, Johannes Gutenberg-Universität Mainz, 55128 Mainz, Germany
  7. Institute of Physics, Czech Academy of Sciences, Prague, Czech Republic
  8. Department of Physics, State Key Laboratory of Surface Physics, Fudan University, Shanghai 200433, China
  9. Shanghai Research Center for Quantum Sciences, Shanghai 201315, China
  10. Institut für Physik, Martin-Luther-Universität, Halle, Germany
- \* E-mail: [lukas.nadvornik@matfyz.cuni.cz](mailto:lukas.nadvornik@matfyz.cuni.cz)

## Abstract

We report on the observation of spin Hall magnetoresistance (SMR) in prototypical bilayers of ferrimagnetic yttrium iron garnet (YIG) and platinum in the frequency range from 0 THz to as high as 1.5 THz. The spectral composition of the effect exhibits a strong low-pass behavior, decreasing by approximately 75% from 0 THz to 0.2 THz and vanishing entirely at 1.5 THz. Using a dynamic magnetoresistive model, we can fully explain the spectral dependence by competition of transverse spin-torque (coherent) and longitudinal (incoherent) contributions to the spin current and their characteristic response times. Our analysis suggests that the slow dissipation of incoherent magnons from the interface is the limiting process responsible for the dramatic spectral decay of the SMR. These results establish THz SMR as a powerful probe of ultrafast interfacial spin-magnon coupling.

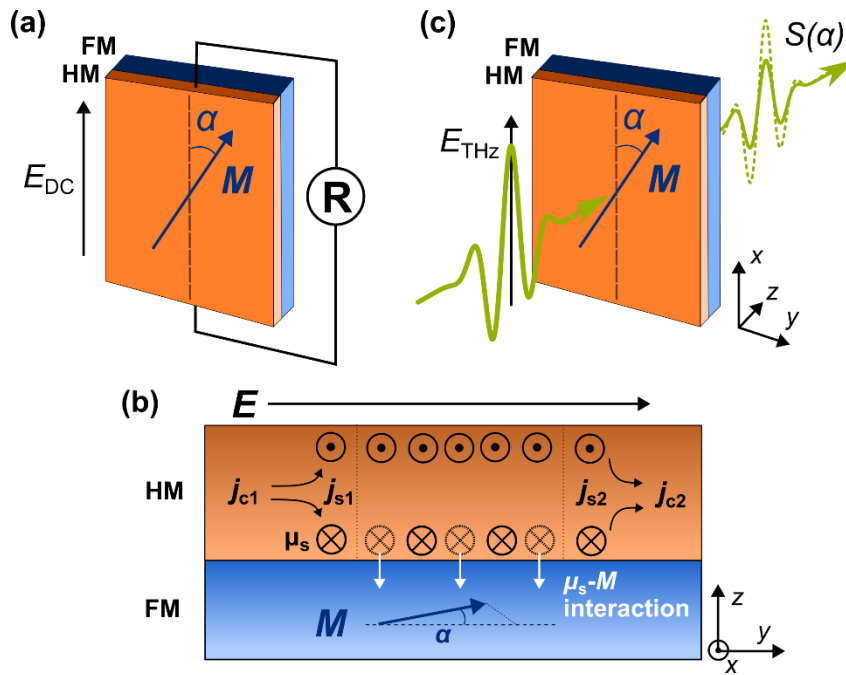


**Figure 1 | Concept of DC and THz SMR.** (a) Electrical contact-based DC transport setup for SMR measurements with the definition of the in-plane angle  $\alpha$  between magnetization  $M$  and applied electric field  $E_{DC}$ . (b) Illustration of the microscopic mechanism of SMR in a FI|HM stack. First, the electric charge current  $j_{c1}$  in the heavy-metal layer (HM) due to an applied electric field  $E$  is converted into a transverse spin current  $j_{s1}$  via the SHE, which leads to a spin accumulation  $\mu_s$  at both HM interfaces (circles). Second, the spin accumulation is partly reduced due to spin relaxation and spin outflow into the ferrimagnetic-insulator layer (FI) via various interactions with  $M$ , which generally depend on orientation of  $M$ . Finally, the remaining spin accumulation leads to a secondary diffusive spin current  $j_{s2}$  and, thus, charge current  $j_{c2}$  via the inverse SHE, which causes a  $M$ -dependent variation of the overall sample resistance  $R$ . (c) Analogous free-space THz setup to (a) with the applied electric field  $E_{THz}$  of a THz pulse, which, following traversal of the sample, is detected as the electro-optical signal  $S(\alpha)$ .

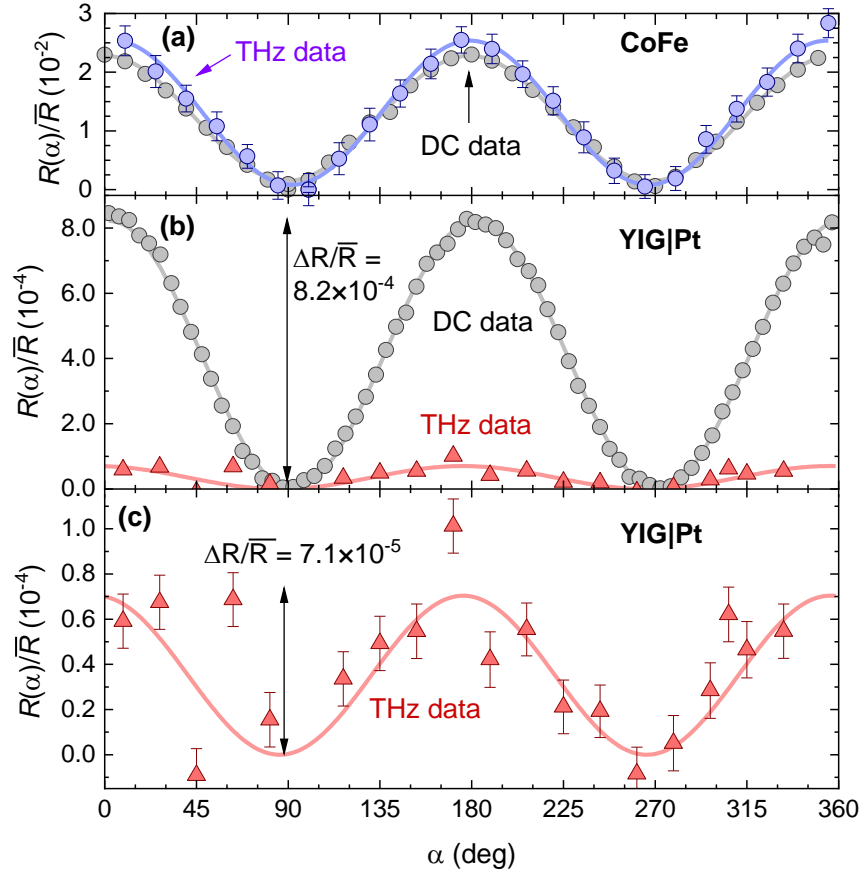


**Figure 2 | Amplitude and  $\alpha$ -dependence of the MR signals.** (a) Test signal of the AMR  $R(\alpha)/\bar{R}$  of CoFe as a function of  $\alpha$  from the DC [grey scatter, Fig. 1(a)] and THz experiments [blue scatter, Fig. 1(c)]. (b) The analogous SMR signal from YIG|Pt(5 nm) in the DC (grey) and THz experiments (red scatter). (c) Magnified THz data of (b). In all panels, the curves are vertically offset to make the absolute minima zero, the solid lines are fits  $\propto \cos^2 \alpha + \text{offset}$  [see Eq. (1)], and arrows indicate the full contrast  $\Delta R/\bar{R}$ .

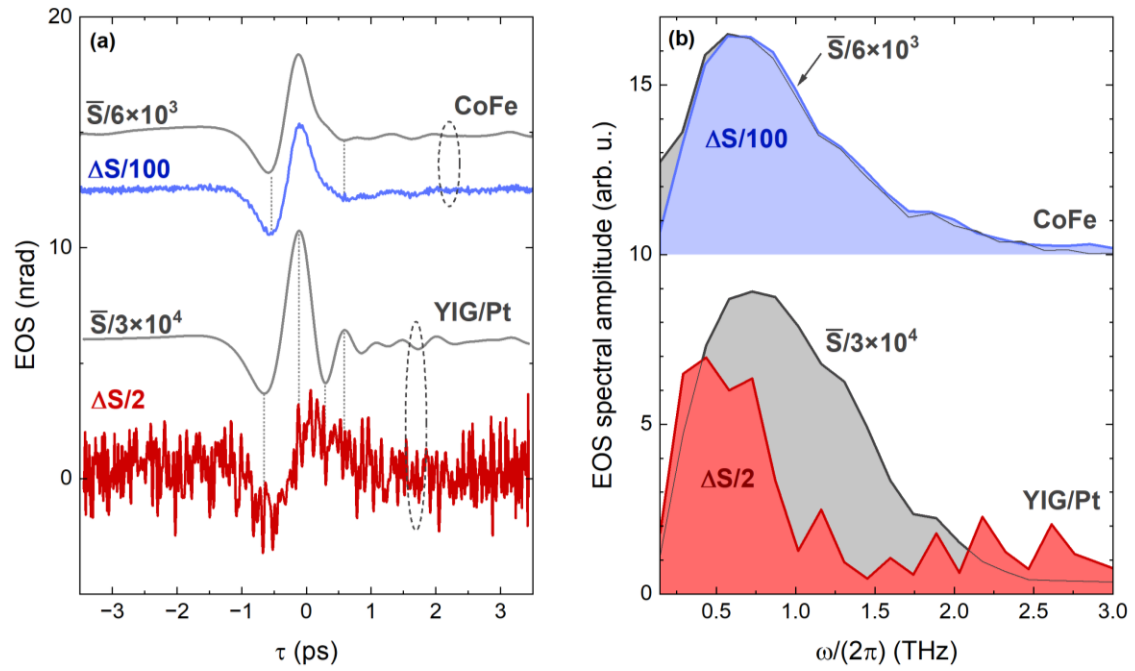


**Figure 3 | THz differential signals.** (a) Measured THz waveforms of the magnetization-independent average transmission  $\bar{S} = (S_{\parallel} + S_{\perp})/2$  (grey curves, rescaled by indicated factor) and the magnetization-dependent differential signals  $\Delta S = S_{\parallel} - S_{\perp}$  for YIG|Pt(5nm) (red) and references CoFe (blue) samples. Dotted lines are guide for the eye. (b) Spectra corresponding to (a), rescaled indicated factors. Curves are shifted vertically for clarity.

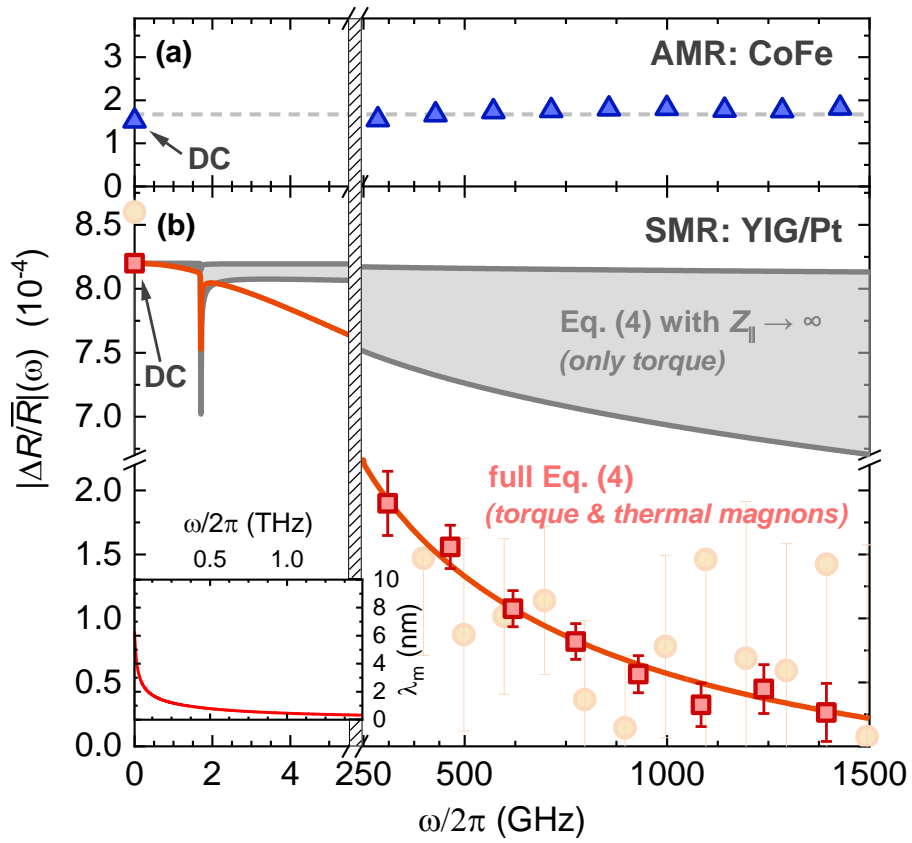


**Figure 4 | Spectrum of MR contrasts.** (a) AMR contrast  $|\Delta R/\bar{R}|$  in reference sample CoFe (blue scatters) as a function of frequency  $\omega/2\pi = 0$ -1.5 THz. The DC value is the electrical measurement at  $\omega = 0$ . (b) Analogous frequency dependence of the SMR contrast  $|\Delta R/\bar{R}|$  of YIG|Pt(5 nm) (red rectangles) and YIG|Pt(3) (yellow circles). Note the split vertical axis. The results of the model [Eq. (4)] for the range of literature values of parameters specified in the text are shown by curves: Eq. (4) with only the torque  $Z_{\perp}$  component (grey curves and shaded area), and Eq. (4) with both  $Z_{\perp}$  and  $Z_{\parallel}$  terms (red curve). Inset: The diffusion length  $\lambda_m(\omega)$  of the magnon accumulation.

The transport of angular momentum by magnons has become a cornerstone of modern spintronics because it does not involve any accompanying charge flow [1]. The spin Hall magnetoresistance (SMR) [2,3,4] has proven to be a powerful tool for studying spin transport in ferro- and antiferromagnetic systems using conventional electrical transport experiments [Fig. 1(a)]. Similar to the anisotropic magnetoresistance (AMR) [5,6], the SMR exhibits in a sample with sufficiently high spatial symmetry the characteristic dependence on the in-plane angle  $\alpha$  between the magnetic order parameter (magnetization  $\mathbf{M}$  or Néel vector) and the electrical current,

$$R(\alpha) = \bar{R} + \Delta R \cos^2 \alpha. \quad (1)$$

Here,  $\bar{R} = (R_{0^\circ} + R_{90^\circ})/2$  is the average of the resistances for  $\alpha = 0^\circ$  and  $90^\circ$ , and  $\Delta R = R_{0^\circ} - R_{90^\circ}$  is their difference.

Unlike AMR, which originates in a single conductive magnetic layer [6,7], the SMR is observed in bilayer structures composed of a heavy-metal layer (HM), such as Pt or W, and a magnetic layer, typically a ferrimagnetic-insulator layer (FI), such as yttrium-iron garnet (YIG), which is the material studied in seminal works on SMR [4,8,9,10,11,12,13] and GdIG [14], but also antiferromagnets, such as the insulator NiO [15] and the altermagnetism candidates  $\text{Fe}_2\text{O}_3$  [16] and  $\text{Ba}_2\text{CoGe}_2\text{O}_7$  [17]. The SMR has also been studied on metallic ferromagnets, like CoFeB [18,19,20]. The current microscopic understanding of the SMR in ferrimagnets [2,21,22,23,24] involves three key spintronic processes [see Fig. 1(b)]: First, the electron current in HM creates a spin accumulation  $\mu_s$  at the HM|FI interface via the spin Hall effect (SHE). Second,  $\mu_s$  is reduced by a spin outflow into FI through various  $\mu_s$ - $\mathbf{M}$  coupling channels whose efficiency depends on the relative orientation of  $\mathbf{M}$  and  $\mu_s$ . Third, the backflow of spin due to the  $\mathbf{M}$ -dependent gradient of  $\mu_s$  along  $z$  is converted into an in-plane charge current via the inverse SHE, which is reflected in a  $\mathbf{M}$ -dependent variation of the longitudinal electrical resistance  $R$ .

Most experimental studies have focused on the transverse torque-type  $\mu_s$ - $\mathbf{M}$  coupling, where  $\mu_s$  is perpendicular to  $\mathbf{M}$  ( $\alpha = 0^\circ$ ) [Fig. 1(b)]. However, recent developments suggest that additional coupling channels, such as via longitudinal incoherent magnons [25,26,27,28,29,30], may also play an important role, especially in insulating systems. It has remained challenging to isolate the contributions of these channels in experiments [Fig.1(b)]. Theory work suggests that these intertwined channels may have a markedly different frequency dependence in the THz range. So far, however, SMR was measured at frequencies 4 GHz [13] and, thus, the efficiency of ultrafast magnon excitation by transient  $\mu_s$  and the frequency-dependent spin-to-magnon coupling remain largely unexplored.

In this letter, we measure THz SMR in the range 0–1.5 THz by DC transport and THz time-domain spectroscopy in the prototypical bilayer system of YIG and platinum. The observed spectral dependence of the SMR is strikingly different from the AMR in reference metallic ferromagnets and exhibit a strong low-pass filter behavior. Comparison to theory indicates that the spin-outflow process in the SMR is governed by a notably slower mechanism as compared to AMR. The modelling analysis suggests that the responsible phenomena is the slow magnon dissipation from the interface.

*Samples.*—Our samples are prototypical SMR bilayers YIG|Pt of the ferrimagnetic insulator  $\text{Y}_3\text{Fe}_5\text{O}_{12}$  (YIG) and the heavy metal Pt. The YIG is grown by liquid-phase epitaxy on (111)-oriented single-crystalline gadolinium garnet substrates (GGG), followed by deposition of Pt by sputtering, forming stacks  $\text{GGG}|\text{YIG}(d_{\text{FI}})|\text{Pt}(d_{\text{HM}})$  with  $d_{\text{FI}} = 630$  nm and  $d_{\text{HM}} = 0, 3, 5$  nm, where  $d_{\text{HM}} = 0$  nm is a control sample. For referencing, we measure the AMR of the model metallic ferromagnets single-crystalline  $\text{Co}_{50}\text{Fe}_{50}$  (10 nm) and polycrystalline  $\text{Ni}_{81}\text{Fe}_{19}$  (8 nm), prepared by molecular-beam epitaxy on a (100)-MgO substrate and by sputtering on a high-resistivity silicon substrate, respectively.

*DC experiments.*—All samples are characterized by measuring the MR contrast in the DC regime in a standard transport setup [Fig. 1(a)], which is equipped with a vector magnet (1 T) [9,11,13]. The example of the resulting variation of normalized resistance  $R(\alpha)/\bar{R}$  with the angle  $\alpha$  for the AMR reference CoFe sample and YIG|Pt(5 nm) is shown in Fig. 2(a) and (b) by grey scatter. Here, the curves are vertically

offset to make the global minimum zero. The data exhibit the characteristic  $\cos^2\alpha$  dependence of the SMR with the contrast  $(\Delta R/\bar{R})_{\text{DC}} = 8.2 \times 10^{-4}$ , as obtained by a fit by Eq. (1), and  $2.3 \times 10^{-2}$  for the AMR contrast of CoFe. Similarly,  $(\Delta R/\bar{R})_{\text{DC}} = 8.6 \times 10^{-4}$  and  $1.1 \times 10^{-2}$  were found for YIG|Pt(3 nm) and NiFe (see Fig. S1) [SuppMat].

*THz experiments.*—The THz measurements are performed in an analogous manner [Fig. 1(c)] to the DC setup [Fig. 1(b)]. The SMR is induced by the electric field of the incident THz pulses, which are generated by optical rectification of femtosecond laser pulses (wavelength 1030 nm, duration 170 fs, energy 50  $\mu\text{J}$ , repetition rate 10 kHz) from a regenerative amplifier in a GaP(110) crystal (thickness 2 mm). After transmission through the sample, the THz electric field is characterized by electrooptic sampling (EOS) in GaP(110) (2 mm), resulting in a signal  $S(t, \alpha)$  as a function of time and  $\alpha$ . Here,  $\alpha$  is the angle between the polarization of the THz pulse and the orientation of  $\mathbf{M}$ , which is set by a rotatable external magnetic field of  $\sim 350$  mT [Fig. 1(c)]. The signal obtained from the reference sample without metal layers is denoted as  $S_{\text{ref}}(t)$ .

By Fourier transformation of the THz signal  $S(t)$ , we obtain its complex-valued Fourier amplitude  $S(\omega)$  and calculate the THz resistance  $R(\omega)$  of the sample stack by the Tinkham formula [7,31,32],

$$R(\omega) = \frac{Z_0}{n(\omega) + 1} \frac{1}{S_{\text{ref}}(\omega)/S(\omega) - 1}. \quad (2)$$

Here,  $Z_0 \approx 377\Omega$  is the vacuum impedance, and  $n(\omega)$  is the refractive index of the substrate (see Note 1 for validity checks) [Suppmat].

To obtain an estimate of the frequency-averaged amplitude of  $R(\alpha, \omega)/\bar{R}(\omega)$ , we approximate  $S_{\text{ref}}(\omega)/S(\omega)$  in Eq. (2) by the ratio of the peak amplitudes of the time-domain waveforms  $S_{\text{ref}}(t)$  and  $S(t)$ . The resulting  $(R(\alpha)/\bar{R})_{\text{THz}}$  is displayed for CoFe and YIG|Pt(5 nm) in Fig. 2(a) and (b). Remarkably, while the AMR contrast  $(\Delta R/\bar{R})_{\text{THz}}$  for CoFe agrees well with that of the DC experiment, we observe one order of magnitude smaller SMR response of YIG|Pt(5 nm),  $(\Delta R/\bar{R})_{\text{THz}} = 7.1 \times 10^{-5}$ , as compared to the DC value [Fig. 2(b) and (c)].

*SMR spectra.*—To further explore this noticeable behavior,  $R(\alpha, \omega)/\bar{R}(\omega)$  needs to be frequency-resolved with sufficient signal-to-noise ratio. To this end, we use a second THz setup in dry-air atmosphere that is driven by low-noise femtosecond laser pulses (wavelength 790 nm, duration 10 fs, energy 2 nJ, repetition rate 80 MHz), another THz emitter (Terablast, Protemics GmbH) and EOS in ZnTe(110) (1 mm). To further enhance the signal-to-noise ratio, we harmonically switch the sample magnetization between the states  $\alpha = 0^\circ$  and  $90^\circ$  at a frequency of 10 kHz with an electromagnet with maximal field 20 mT [7,33], cf. Fig. S2 [Suppmat]. Lock-in-type detection of the resulting signal changes yields the differential signal  $\Delta S = S_{0^\circ} - S_{90^\circ}$ , complemented with the average, magnetization-independent signal  $\bar{S} = (S_{0^\circ} + S_{90^\circ})/2$ . Typical data acquisition times for the SMR samples amounted to 50 h.

Fig. 3 shows  $\Delta S$  and  $\bar{S}$  in the time [panel (a)] and frequency domain [panel (b)] for CoFe and YIG|Pt(5 nm) samples. For the CoFe reference sample, the signals  $\Delta S(t)$  and  $\bar{S}(t)$  have almost identical shape [Fig. 3(a)]. This behavior is consistent with a nearly frequency-independent response of the AMR, as observed previously for Ni, Co, Ni<sub>81</sub>Fe<sub>19</sub> and Ni<sub>50</sub>Fe<sub>50</sub> in the same frequency range 0-3 THz [7,34]. In contrast, the differential signal  $\Delta S(t)$  from YIG|Pt(5 nm) has a much smaller amplitude than that from CoFe and oscillates considerably more slowly [Fig. 3(a)]. Indeed, the amplitude spectrum  $|\Delta S(\omega)|$  is concentrated at lower frequencies [Fig. 3(b)] as compared to  $|\bar{S}(\omega)|$ . This observation suggests that a significantly slower process is involved in the SMR than the AMR, which is governed by electron momentum relaxation with a rate of several 10 THz [7,34]. The very same trend was observed in

YIG|Pt(3 nm) (see Fig. S3) [Suppmat]. Importantly, the signal  $\Delta S(t)$  from the reference YIG sample without Pt is smaller than our detection sensitivity, thereby confirming that the origin of the signal is at the YIG/Pt interface (Fig. S3) [Suppmat].

To infer the THz MR contrast  $(\Delta R/\bar{R})(\omega)$  vs frequency  $\omega/2\pi$  from the data in Fig. 3, we use the relation [7]

$$(\Delta R/\bar{R})(\omega) = \frac{\Delta S(\omega)}{S(\omega)} \left[ 1 + \frac{n(\omega) + 1}{Z_0/\bar{R}(\omega)} \right], \quad (3)$$

where  $\bar{R}$  is the mean THz resistance of the samples, determined by an additional experiment (see Fig. S4) [SupMat]. The magnitude of the resulting THz and DC MR contrast  $\Delta R/\bar{R}(\omega)$  is displayed in Fig. 4 for all samples. As expected from Fig. 3, the AMR is virtually frequency-independent, and its magnitude agrees well with the DC value. In striking contrast, in both YIG|Pt samples, we observe a significant drop of the SMR contrast by more than 75% between 0 THz and 0.2 THz, followed by a further decrease down to the noise floor at 1.5 THz.

*Modeling and discussion.*—The low-pass-type behavior of the SMR contrast  $\Delta R/\bar{R}(\omega)$  must be related to a physical process that is slow compared to the period of our harmonic driving with  $2\pi/\omega \sim 1ps$ . To obtain more insight, we follow the theory of Refs. [23,24]. Here, the SMR is linked to the reduction of the transient spin accumulation  $\mu_s$  in Pt at the Pt/YIG interface due to a spin current  $j_s$  from Pt to YIG [Fig. 1(a)] [4,9,15]. The outflow can be quantified by effective spin impedances  $Z_{\parallel} = \mu_{s\parallel}/j_{s\parallel}$  and  $Z_{\perp} = \mu_{s\perp}/j_{s\perp}$ . Here,  $\mu_{s\parallel}$  and  $\mu_{s\perp}$  is the component of  $\mu_s$  parallel ( $\parallel$ ) and perpendicular ( $\perp$ ) to  $\mathbf{M}$ , respectively, and  $j_{s\parallel}$  and  $j_{s\perp}$  are defined likewise. We note that the perpendicular components  $j_{s\perp}$ ,  $\mu_{s\perp}$ , and  $Z_{\perp}$  are complex, encoding the two spatial directions perpendicular to  $\mathbf{M}$  [23,24]. The SMR contrast [Eq. (1)] is proportional to the difference of the outflows for the cases  $\mathbf{M} \perp \boldsymbol{\mu}_s$  (i.e.,  $\alpha = 0^\circ$ ) and  $\mathbf{M} \parallel \boldsymbol{\mu}_s$  ( $\alpha = 90^\circ$ ), i.e.,

$$(\Delta R/\bar{R})(\omega) = \xi \operatorname{Re} \left( \frac{1}{Z_{\perp}(\omega)} - \frac{1}{Z_{\parallel}(\omega)} \right), \quad (4)$$

where  $\xi$  is a frequency-independent coefficient (see Note 2 in [SupMat] or [23]). Because the observed resistance is higher for  $\alpha = 0^\circ$  than for  $\alpha = 90^\circ$  [Fig. 2(c)], we conclude that the transverse spin channel is dominant, i.e.,  $1/Z_{\perp} > 1/Z_{\parallel}$ .

Therefore, we first consider solely the transverse case ( $\perp$ ) where the spin outflow is due to the spin-torque interaction of  $\mu_s$  and  $M$ . Here, the total outflow is limited by two subsequent processes. ( $\perp$ 1) The transmission of the angular momentum from Pt through the interface into YIG layer is described by the spin-mixing conductance,  $1/Z_{\perp,FI/HM} \propto g_{\uparrow\downarrow}$ , similar to spin-pumping and spin-transfer-torque experiments [35]. It is instantaneous since it is a local interaction where no magnetization dynamics is involved. ( $\perp$ 2) The actual dynamics of  $M$  carries the angular momentum away from the interface into the FI bulk. This process is described by the Landau-Lifshitz-Gilbert equation, and its efficiency scales as  $1/Z_{\perp,FI} \propto \omega^{-1/2}$  for  $\omega \gg \omega_0$ , where  $\omega_0/2\pi \approx 1.7\text{GHz}$  is the resonance frequency of YIG [36]. This behavior is typical for oscillators driven at frequencies above resonance because the oscillator response lags behind the driving force with little transfer of angular momentum. As the processes ( $\perp$ 1) and ( $\perp$ 2) occur sequentially (in series), the total impedance  $Z_{\perp}(\omega)$  equals the sum  $Z_{\perp,FI/HM} + Z_{\perp,FI}(\omega)$ .

To evaluate the impact of  $Z_{\perp,FI}(\omega)$  on SMR, we model the SMR with Eq. (4) and neglect the longitudinal spin channel, i.e.,  $Z_{\parallel}(\omega) \rightarrow \infty$ . We take the explicit formulation of  $Z_{\perp}$  from [23] with literature values of the saturation magnetization  $M_s \approx 140\text{ kA/m}$  for YIG [37], the spin Hall angle  $\theta_{HM} \approx 0.1$  for Pt [9,37] and the measured THz sheet resistance  $R_{HM} = 83\ \Omega$  of the Pt layer using Eq. (2). The spin stiffness  $D_{\text{ex}}$  and the Gilbert damping  $\alpha_G$  of YIG, the spin relaxation length  $\lambda_{HM}$  of Pt and  $g_{\uparrow\downarrow}$  of the FI/HM

interface are kept as free parameters whose values lie in the ranges reported in the literature (see [Table S1](#)) [[Suppmat](#)]. The measured DC value of the SMR contrast is taken as boundary condition. As seen in [Fig. 4\(b\)](#) (grey curves and the shaded area between them), the modeled SMR contrast and, thus, the transverse “torque” component  $Z_{\perp}(\omega)$  cannot capture the strong frequency dependence of our THz data. We, therefore, focus on the longitudinal SMR contributions.

The longitudinal component of SMR,  $Z_{\parallel}(\omega) = Z_{\parallel,FM/HM} + Z_{\parallel,FI}(\omega)$ , is also formed by two sequential processes creating incoherent (thermal) spin fluctuations. (I1) Spin is transmitted through the interface. This process is instantaneous and, thus, implies a frequency-independent  $1/Z_{\parallel,FN}$ . (I2) The angular momentum is carried away from the interface by magnons. The efficiency of this process scales with the gradient of the magnon chemical potential  $\mu_m$  in FI and, thus, with the inverse diffusion length  $1/\lambda_m$  of the magnon population, i.e.,  $1/Z_{\parallel,FI}(\omega) \propto 1/\lambda_m(\omega)$ . By considering the equation of motion for  $\mu_m$ , one can show that (see [Note 3](#)) [[Suppmat](#)]:

$$\lambda_m^2(\omega) \propto \frac{1}{(1 - i\omega\tau)(1 - i\omega\tau_{rel})}. \quad (5)$$

Here,  $\tau$  is the relaxation time of magnon momentum and  $\tau_{rel}$  is the relaxation time of magnon population. Considering that  $\tau$  and  $\tau_{rel}$  are typically of the order of 0.1 ps [[25](#)] and 100 ps [[24](#)] or even 100 ns [[38](#)], respectively, [Eq. \(5\)](#) yields the approximate scaling  $Z_{\parallel,FI}(\omega) \propto \lambda_m(\omega) \propto \omega^{-1/2}$  for  $10 \text{ GHz} < \omega < 10 \text{ THz}$  (see [Notes 2 and 3](#)) [[Suppmat](#)]. Therefore, [Eq. \(5\)](#) potentially provides the observed frequency dependence of the SMR [[Fig. 4\(b\)](#)].

To include this process in our modeling, we fit the whole [Eq. \(4\)](#) to our data [[Fig. 4\(b\)](#)] with the same conditions as above. We obtain excellent agreement of measured data and fit [[Fig. 4\(b\)](#)], and all fit parameters agree well with the ranges reported in literature:  $D_{ex} = 5.3 \times 10^{-6} \text{ m}^2 \text{ s}^{-1}$  [[39](#)],  $\alpha_G = 7 \times 10^{-4}$  [[40](#)],  $\lambda_{HM} = 1.5 \text{ nm}$  [[41](#)],  $g_{\uparrow\downarrow} = (5.1 + 0.3i) \times 10^{14} \text{ } \Omega^{-1} \text{ m}^{-2}$  [[9](#)] (see [Table S1](#) [[Suppmat](#)]). Note that the fit very well captures the frequency dependence of the SMR contrast throughout the covered frequency window 0-1.5 THz. This excellent agreement indicates that the low-pass behavior of the THz SMR cannot be explained without the diffusion of incoherent magnons into the FI bulk which becomes less efficient at frequencies faster than the magnon population relaxation.

The observed vanishing SMR contrast at 1.5 THz is the result of the competition of the transversal, nearly frequency-independent, and longitudinal, frequency-dependent components and their cancellation at this frequency [[Eq. \(4\)](#)]. Since  $1/Z_{\parallel}$  continues to increase with  $\omega$  for larger frequencies, it is expected that the high-THz frequency limit might show non-zero, negative SMR contrast. A change of material parameters, temperature, or magnetic field can possibly lead to a shift of the frequency region where both components cancel. In addition, the resulting  $\lambda_m$  vs  $\omega$  is shown in the inset and indicates that incoherent magnons in YIG have diffusion lengths below 1 nm, which is significantly smaller than the  $\sim 100 \text{ nm}$  inferred from DC experiments [[25,27,28,29,30](#)], in agreement with [Eq. \(5\)](#).

In conclusion, we observed the SMR at frequencies between 0 and 1.5 THz in the prototypical system YIG|Pt with the insulating ferrimagnet YIG. The observed SMR contrast drops by more than 1 order of magnitude as the frequency is increased from 0 THz to 1.5 THz. A dynamic SMR model explains our data very well. It indicates that the relatively small SMR contrast at THz frequencies arises from a partial cancellation of transverse (coherent) and longitudinal (incoherent) contributions to the spin current traversing the interface and the slow diffusion of incoherent magnons from the HM/FI interface. These results establish THz SMR as a powerful probe of ultrafast interfacial spin-magnon coupling and open new avenues for exploring high-frequency spin transport in insulating magnets.

## Acknowledgements

This work was supported by TeraFIT project No. CZ.02.01.01/00/22\_008/0004594 funded by Ministry

of Education Youth and Sports of the Czech Republic (MEYS CR), programme Johannes Amos Comenius (OP JAK), call Excellent Research. The authors acknowledge funding by the Czech Science Foundation (grant no. 21–28876J), by the Grant Agency of the Charles University (grants no. 166123, no. 120324 and SVV–2025–260836), by CzechNanoLab Research Infrastructure supported by MEYS CR (LM2023051), and by MEYS CR project LNSM-LNSpin. The group in Mainz acknowledges funding by the Deutsche Forschungsgemeinschaft (DFG, German Research Foundation) - TRR 173/3 - 268565370 Spin+X (Projects B02,B13, and A01) and the European Union through the Horizon 2020 and HorizonEurope projects under Grant Agreement No. 101070290 (NIMFEIA) and EIC PathfinderOPEN grant 101129641 (OBELIX).

- 
- <sup>1</sup> A. V. Chumak, V. I. Vasyuchka, A. A. Serga, and B. Hillebrands, Magnon spintronics, *Nature Phys* 11, 453 (2015).
- <sup>2</sup> Y.-T. Chen, S. Takahashi, H. Nakayama, M. Althammer, S. T. B. Goennenwein, E. Saitoh, and G. E. W. Bauer, Theory of spin Hall magnetoresistance, *Phys. Rev. B* 87, 144411 (2013).
- <sup>3</sup> W. E. Bailey, A. Ghosh, S. Auffret, E. Gautier, U. Ebels, F. Wilhelm, and A. Rogalev, Pd magnetism induced by indirect interlayer exchange coupling, *Phys. Rev. B* 86, 144403 (2012).
- <sup>4</sup> M. Weiler, M. Althammer, F. D. Czeschka, H. Huebl, M. S. Wagner, M. Opel, I.-M. Imort, G. Reiss, A. Thomas, R. Gross, and S. T. B. Goennenwein, Local Charge and Spin Currents in Magnetothermal Landscapes, *Phys. Rev. Lett.* 108, 106602 (2012).
- <sup>5</sup> T. McGuire and R. Potter, Anisotropic magnetoresistance in ferromagnetic 3d alloys, *IEEE Trans. Magn.* 11, 1018 (1975).
- <sup>6</sup> P. Ritzinger and K. Výborný, Anisotropic magnetoresistance: materials, models and applications, *R. Soc. Open Sci.* 10, 230564 (2023).
- <sup>7</sup> L. Nádvořník, M. Borchert, L. Brandt, R. Schlitz, K. A. de Mare, K. Výborný, I. Mertig, G. Jakob, M. Kläui, S. T. B. Goennenwein, M. Wolf, G. Woltersdorf, and T. Kampfrath, Broadband Terahertz Probes of Anisotropic Magnetoresistance Disentangle Extrinsic and Intrinsic Contributions, *Phys. Rev. X* 11, 021030 (2021).
- <sup>8</sup> S. Y. Huang, X. Fan, D. Qu, Y. P. Chen, W. G. Wang, J. Wu, T. Y. Chen, J. Q. Xiao, and C. L. Chien, Transport Magnetic Proximity Effects in Platinum, *Phys. Rev. Lett.* 109, 107204 (2012).
- <sup>9</sup> M. Althammer, S. Meyer, H. Nakayama, M. Schreier, S. Altmannshofer, M. Weiler, H. Huebl, S. Geprägs, M. Opel, R. Gross, D. Meier, C. Klewe, T. Kuschel, J.-M. Schmalhorst, G. Reiss, L. Shen, A. Gupta, Y.-T. Chen, G. E. W. Bauer, E. Saitoh, and S. T. B. Goennenwein, Quantitative study of the spin Hall magnetoresistance in ferromagnetic insulator/normal metal hybrids, *Phys. Rev. B* 87, 224401 (2013).
- <sup>10</sup> C. Hahn, G. de Loubens, O. Klein, M. Viret, V. V. Naletov, and J. Ben Youssef, Comparative measurements of inverse spin Hall effects and magnetoresistance in YIG/Pt and YIG/Ta, *Phys. Rev. B* 87, 174417 (2013).
- <sup>11</sup> H. Nakayama, M. Althammer, Y.-T. Chen, K. Uchida, Y. Kajiwara, D. Kikuchi, T. Ohtani, S. Geprägs, M. Opel, S. Takahashi, R. Gross, G. E. W. Bauer, S. T. B. Goennenwein, and E. Saitoh, Spin Hall Magnetoresistance Induced by a Nonequilibrium Proximity Effect, *Phys. Rev. Lett.* 110, 206601 (2013).
- <sup>12</sup> N. Vlietstra, J. Shan, V. Castel, B. J. van Wees, and J. Ben Youssef, Spin-Hall magnetoresistance in platinum on yttrium iron garnet: Dependence on platinum thickness and in-plane/out-of-plane magnetization, *Phys. Rev. B* 87, 184421 (2013).
- <sup>13</sup> J. Lotze, H. Huebl, R. Gross, and S. T. B. Goennenwein, Spin Hall magnetoimpedance, *Phys. Rev. B* 90, 174419 (2014).
- <sup>14</sup> B.-W. Dong, J. Cramer, K. Ganzhorn, H. Y. Yuan, E.-J. Guo, S. T. B. Goennenwein, and M. Kläui, Spin Hall magnetoresistance in the non-collinear ferrimagnet GdIG close to the compensation temperature, *J. Phys.: Condens. Matter* 30, 035802 (2018).
- <sup>15</sup> J. Fischer, O. Gomonay, R. Schlitz, K. Ganzhorn, N. Vlietstra, M. Althammer, H. Huebl, M. Opel, R. Gross, S. T. B. Goennenwein, and S. Geprägs, Spin Hall magnetoresistance in antiferromagnet/heavy-metal heterostructures, *Phys. Rev. B* 97, 014417 (2018).
- <sup>16</sup> J. Fischer, M. Althammer, N. Vlietstra, H. Huebl, S. T. B. Goennenwein, R. Gross, S. Geprägs, and M. Opel, Large Spin Hall Magnetoresistance in Antiferromagnetic  $\alpha$ -Fe<sub>2</sub>O<sub>3</sub>/Pt Heterostructures, *Phys. Rev. Applied* 13, 014019 (2020).
- <sup>17</sup> M. Leiviskä et al., Spin Hall magnetoresistance at the altermagnetic insulator/Pt interface, *ArXiv* 2501.19198 (2025).
- <sup>18</sup> J. Kim, P. Sheng, S. Takahashi, S. Mitani, and M. Hayashi, Spin Hall Magnetoresistance in Metallic Bilayers, *Phys. Rev. Lett.* 116, 097201 (2016).
- <sup>19</sup> S. Cho, S. C. Baek, K.-D. Lee, Y. Jo, and B.-G. Park, Large spin Hall magnetoresistance and its correlation to the spin-orbit torque in W/CoFeB/MgO structures, *Sci Rep* 5, 14668 (2015).
- <sup>20</sup> H. Gamou, Y. Du, M. Kohda, and J. Nitta, Enhancement of spin current generation in epitaxial  $\alpha$ -Ta/CoFeB bilayer, *Phys. Rev. B* 99, 184408 (2019).
- <sup>21</sup> Y.-T. Chen, S. Takahashi, H. Nakayama, M. Althammer, S. T. B. Goennenwein, E. Saitoh, and G. E. W. Bauer, Theory of spin Hall magnetoresistance (SMR) and related phenomena, *J. Phys.: Condens. Matter* 28, 103004 (2016).

- 
- <sup>22</sup> X.-P. Zhang, F. S. Bergeret, and V. N. Golovach, Theory of Spin Hall Magnetoresistance from a Microscopic Perspective, *Nano Lett.* 19, 6330 (2019).
- <sup>23</sup> D. A. Reiss, T. Kampfrath, and P. W. Brouwer, Theory of spin-Hall magnetoresistance in the ac terahertz regime, *Phys. Rev. B* 104, 024415 (2021).
- <sup>24</sup> O. Franke, D. Akrap, U. Gems, D. A. Reiss, and P. W. Brouwer, Theory of ac magnetoelectric transport in normal-metal/magnetic-insulator heterostructures, *ArXiv* 2408.13099 (2024).
- <sup>25</sup> L. J. Cornelissen, J. Liu, R. A. Duine, J. B. Youssef, and B. J. van Wees, Long-distance transport of magnon spin information in a magnetic insulator at room temperature, *Nature Phys* 11, 1022 (2015).
- <sup>26</sup> L. J. Cornelissen, K. J. H. Peters, G. E. W. Bauer, R. A. Duine, and B. J. van Wees, Magnon spin transport driven by the magnon chemical potential in a magnetic insulator, *Phys. Rev. B* 94, 014412 (2016).
- <sup>27</sup> D. Wesenberg, T. Liu, D. Balzar, M. Wu, and B. L. Zink, Long-distance spin transport in a disordered magnetic insulator, *Nature Phys* 13, 987 (2017).
- <sup>28</sup> K. An et al., Short-range thermal magnon diffusion in magnetic garnet, *Phys. Rev. B* 103, 174432 (2021).
- <sup>29</sup> S. T. B. Goennenwein, R. Schlitz, M. Pernpeintner, K. Ganzhorn, M. Althammer, R. Gross, and H. Huebl, Non-local magnetoresistance in YIG/Pt nanostructures, *Applied Physics Letters* 107, 172405 (2015).
- <sup>30</sup> J. M. Gomez-Perez, S. Vélez, L. E. Hueso, and F. Casanova, Differences in the magnon diffusion length for electrically and thermally driven magnon currents in  $Y_3Fe_5O_{12}$ , *Phys. Rev. B* 101, 184420 (2020).
- <sup>31</sup> M. Tinkham, Energy Gap Interpretation of Experiments on Infrared Transmission through Superconducting Films, *Phys. Rev.* 104, 845 (1956).
- <sup>32</sup> P. Kubaščík, A. Farkaš, K. Olejník, T. Troha, M. Hývl, F. Krizek, D. C. Joshi, T. Ostatnický, J. Jechumtál, M. Surýnek, E. Schmoranzarová, R. P. Campion, J. Zázvorka, V. Novák, P. Kužel, T. Jungwirth, P. Němec, and L. Nádvořník, Terahertz Probing of Anisotropic Conductivity and Morphology of CuMnAs Epitaxial Thin Films, *Adv. Phys. Res.* 2300075 (2023).
- <sup>33</sup> O. Gueckstock, L. Nádvořník, T. S. Seifert, M. Borchert, G. Jakob, G. Schmidt, G. Woltersdorf, M. Kläui, M. Wolf, and T. Kampfrath, Modulating the polarization of broadband terahertz pulses from a spintronic emitter at rates up to 10 kHz, *Optica* 8, 1013 (2021).
- <sup>34</sup> J.-H. Park, H.-W. Ko, J.-M. Kim, J. Park, S.-Y. Park, Y. Jo, B.-G. Park, S. K. Kim, K.-J. Lee, and K.-J. Kim, Temperature dependence of intrinsic and extrinsic contributions to anisotropic magnetoresistance, *Sci Rep* 11, 20884 (2021).
- <sup>35</sup> Y. Tserkovnyak, A. Brataas, G. E. W. Bauer, and B. I. Halperin, Nonlocal magnetization dynamics in ferromagnetic heterostructures, *Rev. Mod. Phys.* 77, 1375 (2005).
- <sup>36</sup> C. Kittel, *Introduction to Solid State Physics*, 8th ed (Wiley, Hoboken, NJ, 2005).
- <sup>37</sup> M. Weiler, M. Althammer, M. Schreier, J. Lotze, M. Pernpeintner, S. Meyer, H. Huebl, R. Gross, A. Kamra, J. Xiao, Y.-T. Chen, H. Jiao, G. E. W. Bauer, and S. T. B. Goennenwein, Experimental Test of the Spin Mixing Interface Conductivity Concept, *Phys. Rev. Lett.* 111, 176601 (2013).
- <sup>38</sup> S. F. Maehrlein et al., Dissecting spin-phonon equilibration in ferrimagnetic insulators by ultrafast lattice excitation, *Science Advances* 4, eaar5164 (2018).
- <sup>39</sup> S. Klingler, A. V. Chumak, T. Mewes, B. Khodadadi, C. Mewes, C. Dubs, O. Surzhenko, B. Hillebrands, and A. Conca, Measurements of the exchange stiffness of YIG films using broadband ferromagnetic resonance techniques, *J. Phys. D: Appl. Phys.* 48, 015001 (2015).
- <sup>40</sup> S. P. Pati, Influence on the Gilbert damping of yttrium-iron-garnet films by the spin-pumping effect, *Materials Science in Semiconductor Processing* 107, 104821 (2020).
- <sup>41</sup> T. S. Seifert et al., Terahertz spectroscopy for all-optical spintronic characterization of the spin-Hall-effect metals Pt, W and Cu 80 Ir 20, *J. Phys. D: Appl. Phys.* 51, 364003 (2018).

***Supplementary material for***  
**Observation of terahertz spin-Hall  
magnetoresistance in insulating magnet YIG/Pt**

P. Kubaščík<sup>1</sup>, Richard Schlitz<sup>2</sup>, Oliver Gueckstock<sup>3,4</sup>, Oliver Franke<sup>3</sup>, Martin Borchert<sup>5</sup>, Gerhard Jakob<sup>6</sup>, K. Olejník<sup>7</sup>, A. Farkaš<sup>1,7</sup>, Z. Kašpar<sup>1,7</sup>, J. Jechumtál<sup>1</sup>, M. Bušina<sup>1</sup>, E. Schmoranzarová<sup>1</sup>, P. Němec<sup>1</sup>, Martin Wolf<sup>4</sup>, Y. Z. Wu<sup>8,9</sup>, Georg Woltersdorf<sup>10</sup>, Mathias Kläui<sup>6</sup>, Piet W. Brouwer<sup>3</sup>, Sebastian T.B. Goennenwein<sup>2</sup>, Tobias Kampfrath<sup>3,4</sup>, Lukáš Nádvořník<sup>1,\*</sup>

1. Faculty of Mathematics and Physics, Charles University, 121 16 Prague, Czech Republic
  2. Department of Physics, University of Konstanz, Konstanz, Germany
  3. Department of Physics, Freie Universität Berlin, 14195 Berlin, Germany
  4. Department of Physical Chemistry, Fritz Haber Institute of the Max Planck Society, 14195 Berlin, Germany
  5. Max Born Institute for Nonlinear Optics and Short Pulse Spectroscopy, 12489 Berlin, Germany
  6. Institut für Physik, Johannes Gutenberg-Universität Mainz, 55128 Mainz, Germany
  7. Institute of Physics, Czech Academy of Sciences, Prague, Czech Republic
  8. Department of Physics, State Key Laboratory of Surface Physics, Fudan University, Shanghai 200433, China
  9. Shanghai Research Center for Quantum Sciences, Shanghai 201315, China
  10. Institut für Physik, Martin-Luther-Universität, Halle, Germany
- \* E-mail: [lukas.nadvornik@matfyz.cuni.cz](mailto:lukas.nadvornik@matfyz.cuni.cz)

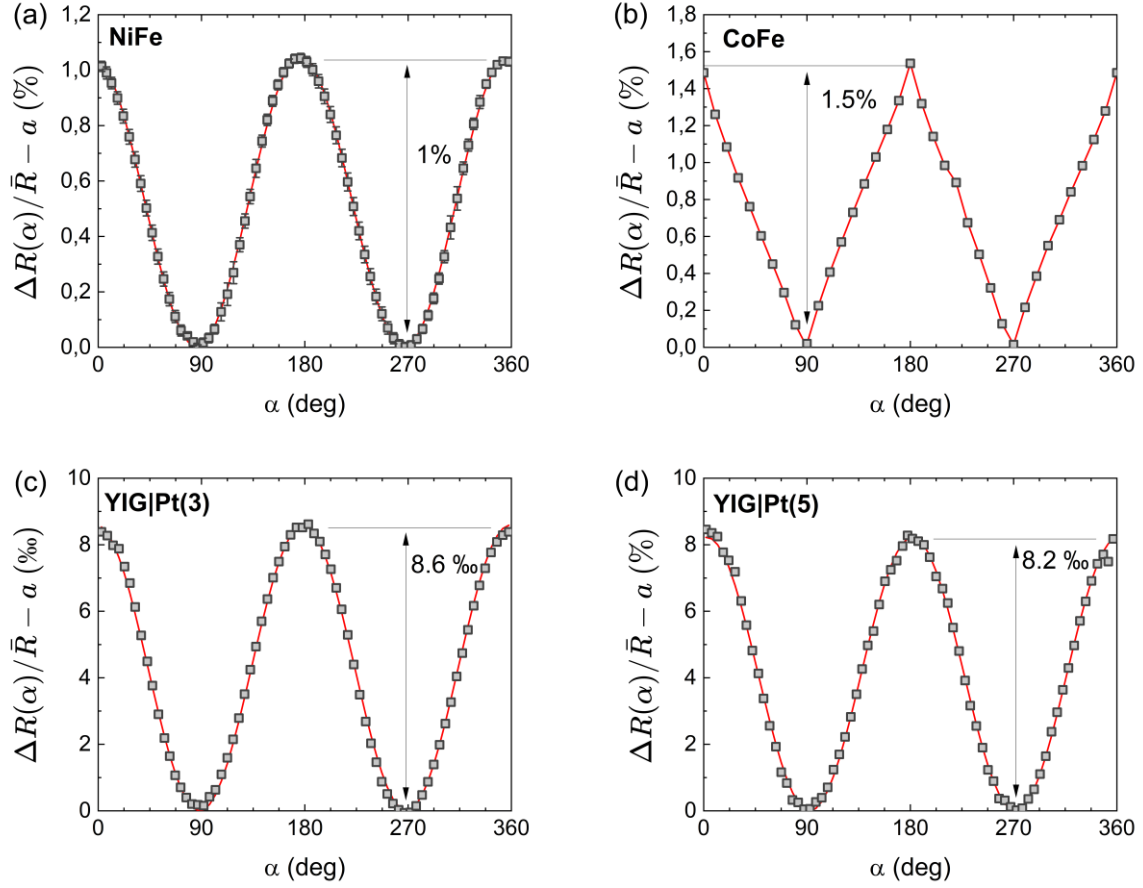


**Fig. S1. DC SMR measurements of YIG/Pt samples.** Scatters correspond to the relative change of resistance  $R(\alpha)/\bar{R} - a$  of (a) NiFe (b) CoFe (c) YIG|Pt(3) and (d) YIG|Pt(5). Red curves are fits by rearranged Eq. (1). Amplitudes of DC AMR(SMR) contrasts are depicted by double-side arrows. Data in (b) were measured with external field of 30 mT to consider that not fully saturated magnetization under these conditions. All other samples were well saturated with 30 mT (see Fig. S2 for YIG and Ref. [2] for NiFe).

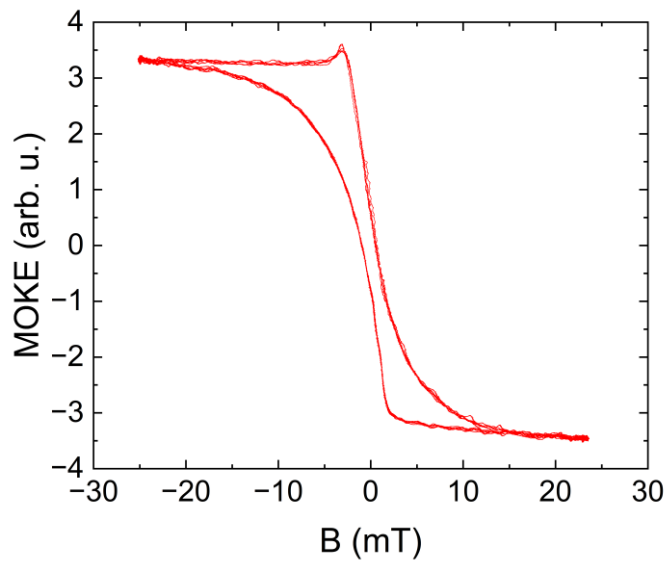


**Fig. S2.** Hysteresis loop measured by the magneto-optical Kerr effect in YIG(5)/Pt sample. The loop indicates the saturation field around 20 mT.

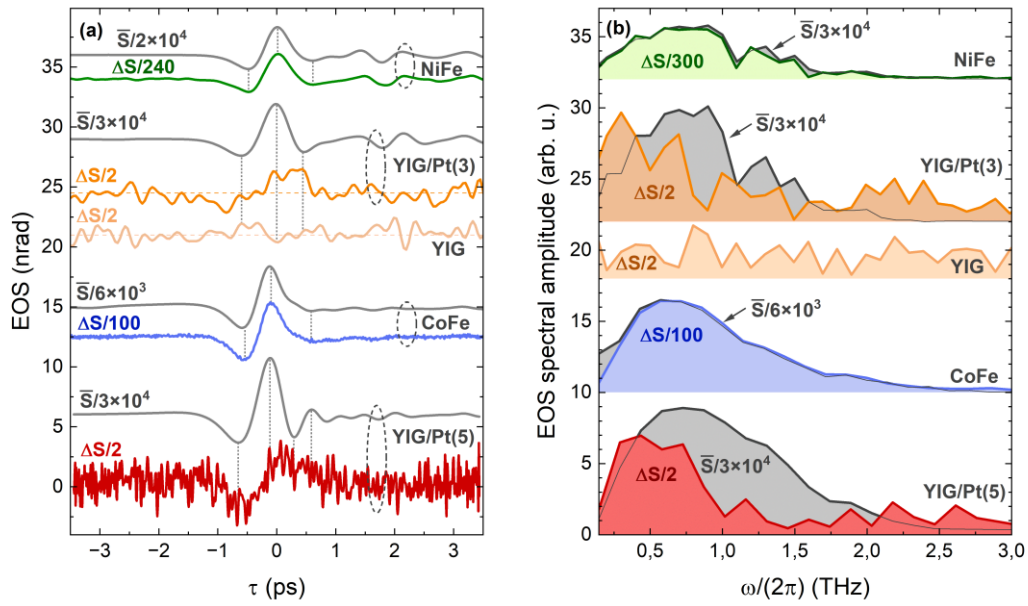


**Figure S3. All measured terahertz signals and corresponding spectra.** (a) Measured THz waveforms of the magnetization-independent average transmission  $\bar{S} = (S_{\parallel} + S_{\perp})/2$  (grey curves, rescaled by indicated factor) and the magnetization-dependent differential signals  $\Delta S = S_{\parallel} - S_{\perp}$  for YIG/Pt(3) (orange curve), YIG/Pt(5) (red) and references NiFe (green) and CoFe samples (blue curve). Dotted lines are guide for the eye. (b) Spectra corresponding to (a), rescaled indicated factors. Curves are shifted vertically for clarity.

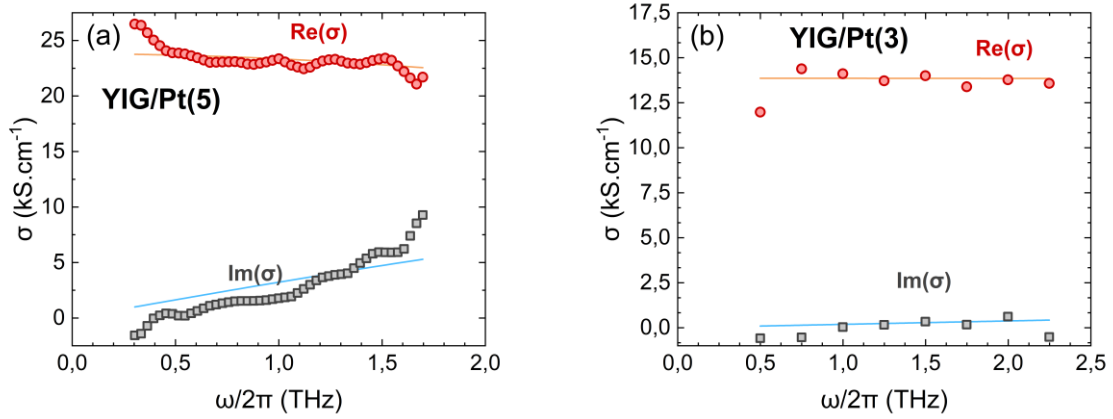


**Fig. S4. THz conductivity of YIG/Pt(5) and YIG/Pt(3).** Red dots (black squares) shows real (imaginary) part of THz conductivity and orange (blue) fit by Drude model of conductivity  $\sigma_0/(1 - i\omega\tau_k)$ , where  $\sigma_0$  is the DC conductivity and  $\tau_k$  is the electron momentum relaxation time. The conductivities of NiFe and CoFe are frequency-independent in our spectral range and reach  $\sigma \approx 2.9 \text{ M}\Omega^{-1}\text{cm}^{-1}$  and  $7.1 \text{ M}\Omega^{-1}\text{cm}^{-1}$ , respectively [1].

<b>Full model</b>		
<b>Fixed parameter</b>	<b>Value</b>	
saturation magnetization of YIG, $M_s$	140 kA/m [2]	
spin Hall angle of Pt, $\theta_N$	0.1 [3]	
resistance of Pt, $R_N$	83 $\Omega$ (measured)	
<b>Free parameter</b>	<b>Range of literature values</b>	<b>Fitted values by Eq. (4)</b>
spin stiffness of YIG, $D_{ex}$	$4 \times 10^{-6} - 1.1 \times 10^{-5} \text{ m}^2 \text{ s}^{-1}$ [2], [4], [5], [6]	$5.3 \times 10^{-6} \text{ m}^2 \text{ s}^{-1}$
Gilbert damping of YIG, $\alpha_G$	$7 \times 10^{-5} - 7 \times 10^{-4}$ [7], [8], [9], [10], [11]	$7 \times 10^{-4}$
spin relaxation length in Pt, $\lambda_N$	1 – 4 nm [2], [3], [12]	1.5 nm
spin-mixing conductance of YIG Pt, $g_{\uparrow\downarrow}$	$5 \times 10^{13} - 9 \times 10^{14} \Omega^{-1} \text{ m}^{-2}$ [2], [3], [7], [13], [14], [15], [16]	$(5.1 + 0.3i) \times 10^{14} \Omega^{-1} \text{ m}^{-2}$
relaxation time, $\tau_m$	247 fs	
<b>Only Torque contribution</b>		
<b>Fixed parameter</b>	<b>Value</b>	
saturation magnetization of YIG, $M_s$	140 kA/m [2]	
spin Hall angle of Pt, $\theta_N$	0.1 [3]	
resistance of Pt, $R_N$	83 $\Omega$ (measured)	
Gilbert damping of YIG, $\alpha$	$1.5 \times 10^{-4}$ (from fit by Full model)	
<b>Free parameter</b>	<b>Lower grey curve</b>	<b>Upper grey curve</b>
spin stiffness of YIG, $D_{ex}$	$4 \times 10^{-6} \text{ m}^2 \text{ s}^{-1}$	$1.1 \times 10^{-5} \text{ m}^2 \text{ s}^{-1}$
spin relaxation length in Pt, $\lambda_N$	1 nm	4 nm
spin-mixing conductance of YIG Pt, $g_{\uparrow\downarrow}$	$9 \times 10^{14} \Omega^{-1} \text{ m}^{-2}$	$3.7 \times 10^{13} \Omega^{-1} \text{ m}^{-2}$

**Tab. S1:** Tables of used material parameters for SMR modelling. The DC value was a boundary condition for the modeling and fitting. Full Eq. (4): The fitted values match well with the range of values reported in literature. Eq. (4) with only the torque contribution ( $Z_{\perp}$ ): The range of literature values was used as limits to fitting intervals, providing a range of results (grey area in Fig. 3) between the best and worst fit (lower and upper grey curves in Fig. 3).

## Notes

### Note 1. Verification of validity of Tinkham formula

Through the whole work, we used Tinkham formula for extraction of conductivity. In this section we will approve its usage by the verification its assumptions [17]. The transmission coefficient  $t(\omega)$  for a thin film deposited in the substrate yields

$$t(\omega) = \frac{E(\omega)}{E_{ref}(\omega)} = \frac{2n(n_s + 1) \exp\left(-\frac{i\omega(n-1)d}{c}\right) \exp\left(-\frac{i\omega(d_s - d_r)(n_s - 1)}{c}\right)}{(n+1)(n_s + n) - (n-1)(n - n_s) \exp\left(-\frac{2i\omega nd}{c}\right)},$$

where  $E(\omega)$  and  $E_{ref}(\omega)$ , are respectively the spectrum of THz wave transmitted through the thin film and substrate. The  $n$  and  $(n_s)$  correspond to refractive index of the thin film (Pt layer) and substrate (YIG,  $n_s = 4.1$  [18]),  $d$  is the thickness of the thin film and  $d_s(d_r)$  thickness of the substrate at the position, where waveform transmitted through Pt layer (substrate) is obtained,  $c$  is the speed of light in vacuum. In the first order of expansion in  $nd$  (the thin film approximation), it follows

$$t(\omega) = \frac{n_s + 1}{n_s + 1 + a + Z_0 \sigma d} \exp(-i\omega \Delta d (n_s - 1)/c),$$

where  $Z_0, \sigma$  are vacuum impedance and THz conductivity of thin film and  $a$  equals to  $\omega n_s d/c$ . In order to use the Tinkham formula, two conditions need to hold: (i)  $n \gg n_s$  and (ii)  $a \ll 1$ . If we assume that there are no interband transitions in the thin film, it gives us the lower estimate for the refractive index. Under this condition, refractive index can be estimated as  $n = \sqrt{1 - i\omega/\sigma \epsilon_0}$ . By taking into account the conductivity of platinum in the YIG|Pt(5) sample,  $\sigma = 2.4 \times 10^6 \text{ Sm}^{-1}$ , the refractive index varies from  $n = 288 - 288i$  at 0.2 THz to  $n = 94 - 94i$  at 2 THz, which is consistent with the literature values[19] This is safely larger than refractive index of YIG in interval 0.2-2 THz and checks condition (i). To verify condition (ii), we calculated the value of the factor  $a$  for the maximal film thickness  $d = 5 \text{ nm}$ , yielding  $a < 0.0013$  for studied spectral range, which fulfils the condition.

## Note 2: THz SMR model and modeling of THz response

In Fig. 4 of the main text, we fit the measured frequency-dependent spin-Hall magnetoresistance using the theory of Ref. [20]. We here describe how the fitted curves were obtained from the theoretical model of Ref. [20].

Reference [20] employs an effective magneto-electric circuit theory similar to that of Ref. [5] for the coupled spin and thermal response to linear order in the electric field  $E(\omega)$  applied in the normal metal NM. In the circuit description, the response of each individual part of the system — the normal-metal layer NM, the magnetic layer M, and their interface — is described with the help of an effective impedance. In a second step, the response of the total system is found using Kirchhoff-like laws to combine these impedances. The impedances relate spin and heat currents to their “driving forces”, which are spin accumulation and temperature for NM and magnon chemical potential and temperature for M [21]. Magnonic relaxation processes are included in the effective impedance of the M layer. The circuit theory of Ref. [20] is the finite-frequency generalization of previous theories of the SMR effect in the low-frequency limit ([22]; [23];[24];[25]).

In the magnet M, the spin current  $j_s$  is carried by magnons. Its components  $j_{s,\perp}$  and  $j_{s,\parallel}$  perpendicular and parallel to the magnetization describe qualitatively different types of magnon response: The transverse component is related to the coherent magnetization dynamics, whereas the longitudinal component describes spin transport by incoherent, thermal magnons. In Ref. [20], the former is described using the Landau-Lifshitz-Gilbert equation, whereas the latter is described by a diffusion-type approach. The relevant parameters describing the M layer in the theory of Ref. [20] are its thickness  $d_M$ , saturation magnetization  $M_s$ , ferrimagnetic resonance frequency  $\omega_0$ , spin stiffness  $D_{ex}$  and Gilbert damping coefficient  $\alpha$ . Further, for spin and heat transport by thermal magnons, Ref. [20] invokes relaxation processes phenomenologically described by the magnon momentum relaxation time  $\tau_m$ , which is dominated by elastic magnon-impurity scattering, as well as the relaxation times  $\tau_{m,ex}$ ,  $\tau_{mp,ex}$ , and  $\tau_{rel}$  for exchange-based magnon-magnon scattering, exchange-based magnon-phonon scattering and spin-nonconserving (relativistic) magnon-phonon and magnon-magnon scattering, respectively.

In Ref. [20] the NM|M interface is described using the spin mixing conductance  $g_{\uparrow\downarrow}$ , which controls the coherent transverse spin current, as well as the incoherent, longitudinal spin current and the heat current through the interface ([26]; [27];[28]). Transport of charge and spin in NM is coupled via the spin-Hall effect and the inverse spin-Hall effect ([29], [30]), which are described phenomenologically using the spin-Hall angle  $\theta_{NM}$ . Spin relaxation of conduction electrons in NM is described phenomenologically with the help of the spin relaxation length  $\lambda_{NM}$ . Other relevant parameters for electron transport in NM are the electrical conductivity  $\sigma_{NM}$  and the thickness  $d_{NM}$  of the NM layer. The theory of Ref. [20] assumes that  $d_{NM} \gg \lambda_{NM}$ , a condition that is satisfied in our experimental setup. Heat currents in NM are described by a diffusion equation, which includes the electronic heat capacity  $C_e$ , the electronic thermal conductivity  $\kappa_e$ , and the electron-phonon relaxation length  $l_{ep}$  as its fundamental parameters.

For a quantitative description of the measured SMR data, we obtain  $\sigma_{NM}$  from the measured resistance of Pt(5),  $R_{NM} = 83 \Omega$ , and we use the actual values for the thicknesses  $d_{NM} = 5 \text{ nm}$  and  $d_M = 630 \text{ nm}$  of the NM and M layers. We estimate the ferrimagnetic resonance frequency  $\omega_0$  by the Kittel formula,  $\omega_0/2\pi = (\gamma/2\pi)\sqrt{\mu_0 H(\mu_0 H + \mu_0 M_s)} \approx 1.75 \text{ GHz}$ , for  $\mu_0 H = 20 \text{ mT}$  and  $\mu_0 M_s = 175 \text{ mT}$ , where we took the well-established literature value for the saturation magnetization of YIG to limit the number of free parameters ([2]). For the material parameters  $\theta_{NM}$ ,  $C_e$ , and  $l_{ep}$ , which describe NM, we also resort to the literature values  $\theta_{NM} = 0.1$ ,  $C_e = 0.13 \times 10^6 \text{ J K}^{-1} \text{ m}^{-3}$ , and  $l_{ep} = 4.5 \text{ nm}$  ([31]; [32]; [3]; [33]; [2][34]). Since the fit was found to be relatively insensitive to the relaxation times  $\tau_{m,ex}$  and  $\tau_{mp,ex}$ , we took literature values  $\tau_{m,ex} = 2.7 \text{ ps}$  ([35]) and  $\tau_{mp,ex} = 0.5 \text{ ps}$  ([21]). The relaxation time for spin-nonconserving relaxation processes  $\tau_{rel}$  is estimated as  $\tau_{rel} \approx \hbar/\alpha k_B T$ . (The same literature values and estimate were used in Ref. [20] for the numerical estimates made there.) The remaining five parameters  $D_{ex}$ ,  $\alpha$ ,  $g_{\uparrow\downarrow}$ ,  $\lambda_{NM}$ , and  $\tau_m$  of the theoretical model are fitted. The fit for the relaxation time  $\tau_m$  was

constrained by the condition that  $80 \text{ fs} < \tau_m < \tau_{\text{mp,el}}$ , where the second inequality follows from the fact that exchange-based magnon-phonon scattering also contributes to magnon momentum relaxation, so that  $\tau_{\text{mp,el}}^{-1}$  is a lower bound for the magnon momentum relaxation rate[20]. The least-squares fit obtained this way very well matches the experimental data (see Fig. 4), whereas the fitted values for  $D_{\text{ex}}$ ,  $g_{\uparrow\downarrow}$ ,  $\alpha$ ,  $\lambda_{\text{NM}}$ ,  $\tau_m$  are within the range of values reported in the literature (see Table S1).

We note that the theory of Ref. [20] (as well as that of Ref. [5]) in general does not imply that  $|\Delta R/\bar{R}| \rightarrow 0$  for  $\omega \rightarrow \infty$ . Rather, it is the difference of coherent/transverse and incoherent/longitudinal magnon transport channels that determines the high-frequency limit of the SMR effect. These depend on material properties and are expected to be different for different material combinations, but also for different temperature or a different applied magnetic field.

In the main text, we also compare our measured data with a theoretical model that includes coherent magnon transport only. This model is obtained from the theory of Ref. [20] by imposing that the longitudinal spin current  $j_{s\parallel}$  through the NM|M interface is zero. To obtain the curves shown in Fig. 4, we took the same value of the Gilbert damping parameter  $\alpha$  as in the fit to the full model. Then, we varied the remaining free parameters within limit intervals with keeping the dc value as the boundary condition. The best and worst match provided by the model within the parameter space are shown by grey curves in Fig. 4 and values of their parameters are given in Table S1. Even the “best” match, which used the extremal values of the parametric space, can not explain the data. Other (non-extremal) combinations of parameters filled the space between the two extremal curves (grey-shaded area in Fig. 4).

### Note 3: Derivation of $\lambda_m(\omega)$

We express  $\lambda_m(\omega)$  using the constitutive propagation equation for magnons:

$$\partial_t \mu_m - \frac{\sigma_m}{1 - i\omega\tau_m} \nabla^2 \mu_m + \frac{\mu_m}{\tau_{\text{rel}}} = 0,$$

where  $\sigma_m$  is the magnon conductivity,  $\tau_m$  the relaxation time of magnon momentum as obtained from Matthias rule from all contributing spin-conserving scattering processes, and  $\tau_{\text{rel}}$  the relaxation time of the magnon population, given by the spin non-conserving scattering [20]. By rewriting the above equation into the general form of spin-diffusion,

$$\nabla^2 \mu_m = \lambda_m^{-2} \mu_m$$

yields the proportionality

$$\lambda_m^{-2}(\omega) \propto (1 - i\omega\tau_m)(1 - i\omega\tau_{\text{rel}}),$$

i.e., Eq. (5) of the main text.

## References

- [1] L. Nádorník *et al.*, “Broadband terahertz probes of anisotropic magnetoresistance disentangle extrinsic and intrinsic contributions,” *Phys Rev X*, vol. 11, no. 2, p. 021030, 2021.
- [2] M. Weiler *et al.*, “Experimental test of the spin mixing interface conductivity concept,” *Phys Rev Lett*, vol. 111, no. 17, p. 176601, 2013.
- [3] M. Althammer *et al.*, “Quantitative study of the spin Hall magnetoresistance in ferromagnetic insulator/normal metal hybrids,” *Physical Review B—Condensed Matter and Materials Physics*, vol. 87, no. 22, p. 224401, 2013.
- [4] C. M. Srivastava and R. Aiyar, “Spin wave stiffness constants in some ferrimagnetics,” *Journal of Physics C: Solid State Physics*, vol. 20, no. 8, p. 1119, 1987.
- [5] D. A. Reiss, T. Kampfrath, and P. W. Brouwer, “Theory of spin-Hall magnetoresistance in the ac terahertz regime,” *Phys Rev B*, vol. 104, no. 2, p. 024415, 2021.
- [6] S. Klingler *et al.*, “Measurements of the exchange stiffness of YIG films using broadband ferromagnetic resonance techniques,” *J Phys D Appl Phys*, vol. 48, no. 1, p. 015001, 2014.
- [7] M. Haertinger *et al.*, “Spin pumping in YIG/Pt bilayers as a function of layer thickness,” *Phys Rev B*, vol. 92, no. 5, p. 054437, 2015.
- [8] L. Siegl *et al.*, “Inductive noise spectroscopy of thermally excited magnons,” *Phys Rev Appl*, vol. 22, no. 5, p. 054036, 2024.
- [9] S. P. Pati, “Influence on the Gilbert damping of yttrium-iron-garnet films by the spin-pumping effect,” *Mater Sci Semicond Process*, vol. 107, p. 104821, 2020.
- [10] S. P. Pati, “Study on the Gilbert damping of polycrystalline YIG films with different capping layers,” *Current Applied Physics*, vol. 20, no. 1, pp. 167–171, 2020.
- [11] C. Hauser *et al.*, “Yttrium iron garnet thin films with very low damping obtained by recrystallization of amorphous material,” *Sci Rep*, vol. 6, no. 1, p. 20827, 2016.
- [12] S. Keller *et al.*, “Determination of the spin Hall angle in single-crystalline Pt films from spin pumping experiments,” *New J Phys*, vol. 20, no. 5, p. 053002, 2018.
- [13] S. R. Marmion, M. Ali, M. McLaren, D. A. Williams, and B. J. Hickey, “Temperature dependence of spin Hall magnetoresistance in thin YIG/Pt films,” *Phys Rev B*, vol. 89, no. 22, p. 220404, 2014.
- [14] K. Uchida, Z. Qiu, T. Kikkawa, R. Iguchi, and E. Saitoh, “Spin Hall magnetoresistance at high temperatures,” *Appl Phys Lett*, vol. 106, no. 5, 2015.
- [15] C. Hahn, G. De Loubens, O. Klein, M. Viret, V. V. Naletov, and J. Ben Youssef, “Comparative measurements of inverse spin Hall effects and magnetoresistance in YIG/Pt and YIG/Ta,” *Physical Review B—Condensed Matter and Materials Physics*, vol. 87, no. 17, p. 174417, 2013.

- [16] Z. Qiu *et al.*, “Spin mixing conductance at a well-controlled platinum/yttrium iron garnet interface,” *Appl Phys Lett*, vol. 103, no. 9, 2013.
- [17] P. Kubaščík *et al.*, “Terahertz probing of anisotropic conductivity and morphology of CuMnAs epitaxial thin films,” *Advanced Physics Research*, vol. 3, no. 1, p. 2300075, 2024.
- [18] Y.-L. Li, T.-F. Li, Q.-Y. Wen, F. Fan, Q.-H. Yang, and S.-J. Chang, “Terahertz magneto-optical effect of wafer-scale La: yttrium iron garnet single-crystal film with low loss and high permittivity,” *Opt Express*, vol. 28, no. 14, pp. 21062–21071, 2020.
- [19] V. Unikandanunni, F. Rigoni, M. C. Hoffmann, P. Vavassori, S. Urazhdin, and S. Bonetti, “Ultrafast electron dynamics in platinum and gold thin films driven by optical and terahertz fields,” *Appl Phys Lett*, vol. 120, no. 2, p. 021601, Jan. 2022, doi: 10.1063/5.0068086.
- [20] O. Franke, D. Akrap, U. Gems, D. A. Reiss, and P. W. Brouwer, “Theory of ac magnetoelectric transport in normal-metal  $\delta$ - $\delta$  magnetic-insulator heterostructures,” *arXiv preprint arXiv:2408.13099*, 2024.
- [21] L. J. Cornelissen, K. J. H. Peters, G. E. W. Bauer, R. A. Duine, and B. J. van Wees, “Magnon spin transport driven by the magnon chemical potential in a magnetic insulator,” *Phys Rev B*, vol. 94, no. 1, p. 014412, 2016.
- [22] Y.-T. Chen *et al.*, “Theory of spin Hall magnetoresistance,” *Physical Review B—Condensed Matter and Materials Physics*, vol. 87, no. 14, p. 144411, 2013.
- [23] Y.-T. Chen *et al.*, “Theory of spin Hall magnetoresistance (SMR) and related phenomena,” *Journal of Physics: Condensed Matter*, vol. 28, no. 10, p. 103004, 2016.
- [24] X.-P. Zhang, F. S. Bergeret, and V. N. Golovach, “Theory of spin Hall magnetoresistance from a microscopic perspective,” *Nano Lett*, vol. 19, no. 9, pp. 6330–6337, 2019.
- [25] X. Wang, Z. Zhou, Y. Nie, Q. Xia, and G. Guo, “Self-consistent study of local and nonlocal magnetoresistance in a YIG/Pt bilayer,” *Phys Rev B*, vol. 97, no. 9, p. 094401, 2018.
- [26] A. Brataas, Y. V. Nazarov, and G. E. W. Bauer, “Finite-element theory of transport in ferromagnet–normal metal systems,” *Phys Rev Lett*, vol. 84, no. 11, p. 2481, 2000.
- [27] J. Xiao, G. E. W. Bauer, K. Uchida, E. Saitoh, and S. Maekawa, “Theory of magnon-driven spin Seebeck effect,” *Physical Review B—Condensed Matter and Materials Physics*, vol. 81, no. 21, p. 214418, 2010.
- [28] S. A. Bender and Y. Tserkovnyak, “Interfacial spin and heat transfer between metals and magnetic insulators,” *Phys Rev B*, vol. 91, no. 14, p. 140402, 2015.
- [29] M. I. Dyakonov and V. I. Perel, “Current-induced spin orientation of electrons in semiconductors,” *Phys Lett A*, vol. 35, no. 6, pp. 459–460, 1971.
- [30] J. E. Hirsch, “Spin hall effect,” *Phys Rev Lett*, vol. 83, no. 9, p. 1834, 1999.

- [31] Z. Lin, L. V Zhigilei, and V. Celli, "Electron-phonon coupling and electron heat capacity of metals under conditions of strong electron-phonon nonequilibrium," *Physical Review B—Condensed Matter and Materials Physics*, vol. 77, no. 7, p. 075133, 2008.
- [32] S. E. Sullivan, H. Lee, A. Weathers, and L. Shi, "Frequency-dependent phonon-mediated unidirectional magnetoresistance in a metal on an insulator with highly nonequilibrium magnons," *Phys Rev B*, vol. 107, no. 14, p. L140412, 2023.
- [33] J. Flipse, F. K. Dejene, D. Wagenaar, G. E. W. Bauer, J. Ben Youssef, and B. J. Van Wees, "Observation of the spin Peltier effect for magnetic insulators," *Phys Rev Lett*, vol. 113, no. 2, p. 027601, 2014.
- [34] J. Rumble, *CRC handbook of chemistry and physics*, vol. 102. CRC press Boca Raton, FL, 2017.
- [35] Z. Shi *et al.*, "Role of magnon-magnon scattering in magnon polaron spin Seebeck effect," *Phys Rev Lett*, vol. 127, no. 27, p. 277203, 2021.